Computational resource advantage of an ion trap quantum classifier

Tarun Dutta,^{1,*} Adrián Pérez-Salinas,^{2,3} Jasper Phua Sing Cheng,¹ José Ignacio Latorre, ^{1,4,5} and Manas Mukherjee^{1,6,7,†}

¹Centre for Quantum Technologies, National University of Singapore, Singapore 117543

²Barcelona Supercomputing Center, Barcelona 08034, Spain

³Departament de Física Quàntica i Astrofísica and Institut de Ciències
del Cosmos, Universitat de Barcelona, Barcelona 08028, Spain

⁴Qilimanjaro Quantum Tech, Barcelona 08007, Spain

⁵Quantum Research Centre, Technology Innovation Institute, P.O.Box: 9639, Abu Dhabi, United Arab Emirates

⁶MajuLab, International Joint Research Unit UMI 3654, CNRS, Université Côte d'Azur, Sorbonne
Université, National University of Singapore, Nanyang Technological University, Singapore

⁷Center for Quantum Engineering Research and Education, TCG CREST, Techna, Sector V, Kolkata 700091, India

Quantum computers can provide solutions to classically intractable problems but only in a handful of cases, this can be proved rigorously. However, in the setting of limited computation resources, there exist many examples where provable theoretical advantage can be achieved and was demonstrated experimentally in handful of realizations. Here we experimentally demonstrate the quantum advantage in a machine learning problem with the limited resources in an ion-trap based quantum processing unit. This versatile quantum classifier uses the data re-uploading supervised machine learning algorithm to train in two steps: first, the quantum circuit is fed with an optimal set of variational parameters found by a classical simulation; then, the variational circuit is optimized by inspecting the parameter landscape with only the quantum processing unit. This second step provides a partial cancellation of the systematic errors inherent to the quantum device. The accuracy of our quantum supervised classifier is benchmarked on a variety of datasets, that implies, finding the separation of the classes associated to regions in a plane in both binary and multi-class problems, as well as in higher-dimensional feature spaces. Our experiments show that a single-ion quantum classifier circuit made out of k gates is at least as powerful as a neural network with one intermediate hidden layer of k neurons. However, in this computational resource-restricted setup with only one qubit, the neural network is computationally more expensive as each neuron needs N gates to approximate a non-linear (mostly Sigmoid) function which is reversibly done by a single rotation in the qubit space. Therefore, the demonstration of a competing quantum classifier will open further possibilities to explore the real usage of a small-scale quantum processor showing advantages in physical resource requirements like the number of gates.

INTRODUCTION

Quantum computing is an active field of research both in academics and industry. It is expected that quantum computers will provide solutions to classically intractable problems. A handful of problems has been found for which quantum computers can provide a solution with a certain, even exponential, speed-ups with respect to a classical computer [1–5]. On the experimental side, recent advances have achieved quantum supremacy, that is, solving a problem in a quantum computer more efficiently and accurately than using classical methods. This has been demonstrated both in superconducting [6] and photonic [7, 8] platforms. Data classification is an ubiquitous problem appearing across many different fields. Classical machine learning provides a plethora of algorithms for this purpose, notably those related to support vector machines [9] or neural networks [10, 11]. In recent years, classical machine learning has improved substantially and can now provide solutions to a large variety of classification problems [12, 13]. These classical algorithms are generally implemented using specialized software and hardware that are expensive in both computational and energy resources.

Quantum Machine Learning (QML) aims to combine the spirits of classical machine learning and the capabilities of quantum computing. This field of research is still in an early stage and, in general, cannot compete against the state-of-the-art classical algorithms. However, recent theoretical works have proven quantum advantages in selected problems [14]. Nowadays, most QML algorithms rely on variational methods [15–18], where theoretical arguments assessing the power of quantum devices are still missing. Variational quantum algorithms are believed

to fit the requirements of Noisy Intermediate-Scale Quantum (NISQ) devices [19], motivating the use of these methods for the early experiments of QML.

Experiments towards developing QML applications in the NISQ era have progressed in different platforms. Photonic devices achieved one of the earliest experiments for addressing a classification problem [20] based on Quantum Support Vector Machines (QSVM) [21]. Superconducting qubits have addressed QML using variational algorithms [22]. The strength of a trapped ion platform lies in the accurate control of small systems [23, 24].

In this paper we implement a QML algorithm on an ion-trap quantum device. Trapped ions are an alternative design of quantum devices whose main strength relies on the accurate control of small quantum systems. Recent experiments have widened the range of feasible experiments [25–28]. The QML algorithm chosen for this application is *data re-uploading* [29, 30]. The main reason for this choice is that data re-uploading is a method specifically designed to take advantage of the Hilbert space available in quantum systems with few qubits. Thus, in order to attain good performances it is necessary to execute highly accurate quantum operations.

The data re-uploading technique is a general scheme for supervised learning in QML using classical data. It was originally conceived as a quantum classifier [30]. The differentiating characteristic of this method is that the data is re-uploaded several times along the computation process. The performance of this algorithm improves as the query complexity, that is the number of data re-uploading, increases. The theoretical capability of this model to approximate any function is guaranteed and emerges from its quantum nature [29, 31].

In this paper, we experimentally demonstrate computing resource advantage of an ion trap quantum classifier for supervised learning, and use it to solve a variety of classification problems. The quantum machine we use is based on a single trapped ion operating up to ~ 15 consecutive gates, that we refer as a Quantum Processing Unit (QPU).

The data re-uploading technique relies less on the width but more on the depth of the circuit, making it suited to run a competitive quantum classifier on a small but precise ion trap based quantum computer [32, 33]. The data re-uploading scheme was also tested on classical simulators with noise models [34]. However, a classical simulator does not necessarily capture the merits and demerits of a real QPU. Indeed, a classical simulator is agnostic to the QPU platform specificity, such as its native gates, and noise models are also platform dependent. The experimental approach presented in this work is, to the best of our knowledge, the first successful experimental implementation of the re-uploading scheme for quantum classifiers with a single-qubit quantum processor.

More specifically, in this work we classify points in a multi-dimensional feature space, where the classes are defined by geometrical figures. The examples provided here have an increasing level of difficulty. We start with a simple binary classification, namely samples inside and outside a circle. We then proceed to deal with more difficult problems, including non-convex and disjoint non-simply connected classes, a variety of geometrical shapes, and increasing dimension of the feature spaces. The classification task is successfully accomplished by the same ion trap QPU in all the cases.

The paper is structured as follows: Sec. *Results* compares the result of the experiment to the ideal simulation results. The observed commonalities and differences between the various datasets is vividly discussed in Sec. *Discussion*. The methods and techniques used to arrive at the results that are shown in this article are presented in Sec. *Methods*.

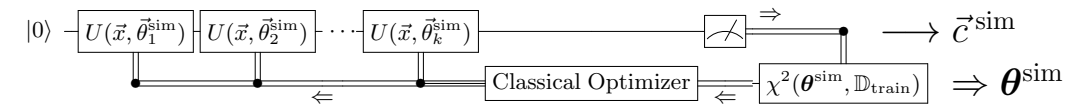
RESULTS

Here, we show the final results for various classification problems represented by different datasets. The results are sequentially presented with increasing level of difficulty in classification. For each classification problem, We compare the performance of the single qubit classifier run on the QPU against a competing classical simulation of the same data. A succinct description of the quantum hardware and the theoretical scheme used in this work to classify data is provided in the following for easy understanding of the results. An in-depth discussion about the experiment and the theory behind data re-uploading is given in the *Methods* section.

The qubit is realized in the two electronic states of a barium ion coupled by an electric quadrupole transition operated at 1762 nm wavelength. The ion is confined in a linear blade trap operating at a radial frequency of

Quantum classifier: multi-variable $\vec{x} \Rightarrow$ multi-class \vec{c}

1. TRAINING USING CLASSICAL SIMULATION



2. TRAINING USING QUANTUM PROCESSING UNIT

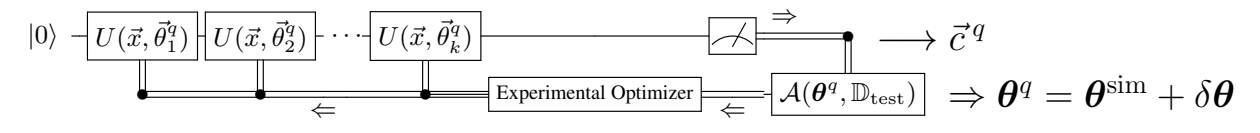


FIG. 1. Schematic description of the training algorithm used in this work. In a first step, data re-uploading is trained using a classical simulation. The simulated quantum circuit is composed of single-qubit gates U that depend on variational parameters θ and the variables \vec{x} associated to a given pattern. The output state is measured to obtain a vector \vec{c} encoding the probabilities that will serve to classify the given pattern into a category. A classical optimization is performed to obtain optimal values θ^{sim} . This optimization is driven by the cost function χ^2 evaluated on training data, $\mathbb{D}_{\text{train}}$. In a second step, a further optimization is accomplished only using the quantum device, taking as starting point the values θ^{sim} and delivering a better set θ^q . The quantity which is now maximized is the accuracy \mathcal{A} evaluated on the test dataset \mathbb{D}_{test} . The aim of the experimental optimization is to mitigate and even compensate possible systematic experimental errors.

1.5 MHz and an axial frequency of 0.3 MHz. Laser cooling of the ion to the Doppler limit, ensures that the qubit is not influenced by the external motion. The most relevant parameters of the trapped ion in this experiment are the qubit coherence time and the Rabi π -time of the qubit. The former is about 5 ms while the later is about $12~\mu s$ [35, 36]. In order to avoid accumulation of phase noise, during the on-off time of the laser, radio-frequency (RF) pulse shaping has been implemented at the RF switch before being fed to the acousto-optic modulator (AOM) for switching. All the RF sources are synchronized to a rubidium atomic clock to obtain phase noise well below 0.01%. The contribution from other systematic errors are discussed in Sec. *Methods*.

In general, the classification algorithm requires the repetition of any pair of non-commuting rotational gates, see Sec. Methods for further details. We chose R_z and R_y , instead of the active gates of the ion qubit R_x and R_y . Active rotations are realized by the application of resonant laser at the qubit frequency applied for a duration proportional to the rotation angle. On the other hand, R_z can be implemented by a combination of the other two active gates or by varying the qubit energy [37, 38]. Both these methods are error prone as the qubit-light interaction is switched on for certain time. We chose instead to perform the R_z by changing the laser phase without interacting with the ion [39], thus the resultant error is limited by only the R_y gate in each layer. Furthermore, every $R_z(\phi)$ gate followed by a $R_y(\theta)$ gate can be concatenated to a single gate $R_\phi(\theta)$ representing a qubit rotation, in a Bloch sphere representation, about the $(\phi,0)$ axis by angle θ . Here, the Bloch vectors are represented in the spherical polar coordinates (ϕ,θ) and hence the rotation operator is equivalently represented as $R_\phi(\theta) \equiv R(\phi,\theta)$. The concatenation makes the effective circuit depth half of the original.

The quantum algorithm here presented delivers an output quantum state

$$|\psi(\vec{x}, \boldsymbol{\theta})\rangle = \prod_{i=1}^{L} U(\vec{x}, \vec{\theta}_i) |0\rangle$$
 (1)

where each $U(\vec{x}, \vec{\theta_i})$ is referred to as a layer and depends on both sampling data \vec{x} and tunable parameters $\vec{\theta_i}$, with

 $\theta = \{\vec{\theta}_1, \vec{\theta}_2, \dots, \vec{\theta}_L\}$. Each layer is composed by R_y and R_z , see Sec. Methods for further details. As we aim to build a classifier for supervised learning, each sample \vec{x} in the dataset is associated to a class within the set \vec{c} . We must also define as many label states $|\phi_c\rangle$ as existing classes. Then, the probability of a state corresponding to a class $c \in \vec{c}$ corresponds to

$$\operatorname{Prob}(\vec{x}, \boldsymbol{\theta} | c) = \frac{\left| \left\langle \phi_c | \psi(\vec{x}, \boldsymbol{\theta}) \right\rangle \right|^2}{\sum_{c'} \left| \left\langle \phi_{c'} | \psi(\vec{x}, \boldsymbol{\theta}) \right\rangle \right|^2}.$$
 (2)

This probability assignment needs to choose a target ket $|\phi_c\rangle$ for each class in every different problem considered considered here. The general rule is to choose the target kets as distant as possible from each other, to maximize the distinguishability among the classes. Given the output from the quantum computer, a final class c is assigned to a given pattern according to the target ket that receives the largest probability. That is, the estimator \bar{c} corresponds to the class with largest probability

$$\bar{c} = \arg\max_{c} \text{Prob}(\vec{x}, \boldsymbol{\theta}|c).$$
 (3)

For the algorithm to work properly it is necessary to find the configuration of parameters θ such that the fidelity between the output states and their corresponding label states are in average maximum for all patterns in the training dataset, $\{\vec{x},c\} \in \mathbb{D}_{\text{train}}$. For a training dataset with N_{train} patterns, the loss function describing this behavior is just a χ^2

$$\chi^2(\boldsymbol{\theta}; \mathbb{D}_{\text{train}}) = \frac{1}{N_{\text{train}}} \sum_{D_{\text{train}}} (c - \bar{c})^2, \qquad (4)$$

where, θ^{sim} being the optimal configuration of parameters that minimizes this χ^2 . For the sake of clarity, we have added a superscript in θ^{sim} that indicates that these parameters are those obtained as a result of the simulation step. The classical optimization can be done using standard optimizers such as those in [40, 41].

The performance of supervised-learning models is not measured by its capability to learn the training dataset, but its generalization power. Then, the quantity of interest is the accuracy \mathcal{A} . This quantity is measured over sampled on an unlearned dataset that we denote as D_{test} . The validation process in machine learning can be refined to be made of training, validation and test. We here stick to only two steps. Therefore, in our case, the accuracy of the classifier is defined as

$$\mathcal{A}(\boldsymbol{\theta}; \mathbb{D}_{\text{test}}) = \frac{\text{Correct guesses}}{\text{Total patterns}},\tag{5}$$

which is bounded between 0 and 1, being 1 the optimal result. There are now three possibilities to test our classifier. We can validate the quantum circuit as follows: *i)* Run an exact simulation of the quantum circuit with the optimal parameters θ^{sim} and label its accuracy as \mathcal{A}^* ; *ii)* Run the QPU with the same parameters θ^{sim} , do sampling of outcomes and label the accuracy as \mathcal{A}^{sim} ; *iii)* finally, improved the results allowing the QPU to look for better variational parameters θ^{q} than those predicted classically and label the accuracy as \mathcal{A}^{q} .

For every classification problem we validate the exact simulation of the circuit on the test set. Therefore, for every experiment we know what the target \mathcal{A}^* is. This can be compared with genuinely classical optimizers based on e. g. neural networks. For the first experimental validation test, we inject the optimal parameters obtained in the simulation step into the QPU. Thus we use the notation QPU(θ^{sim}), since the QPU is fed with the angles that were obtained by classical simulation. It is expected that experimental errors will deteriorate the ideal performance of the computer. This is the case, indeed, but we shall shortly see that results remain very competitive in the experimental setup.

A relevant improved quantum classifier can be obtained doing a new step of training as shown in Fig. (1). This further optimization step is carried on the QPU starting from the simulated results, but exploring the parameter space around the ideal point. As a matter of fact, this procedure leads to a new set of optimized parameters

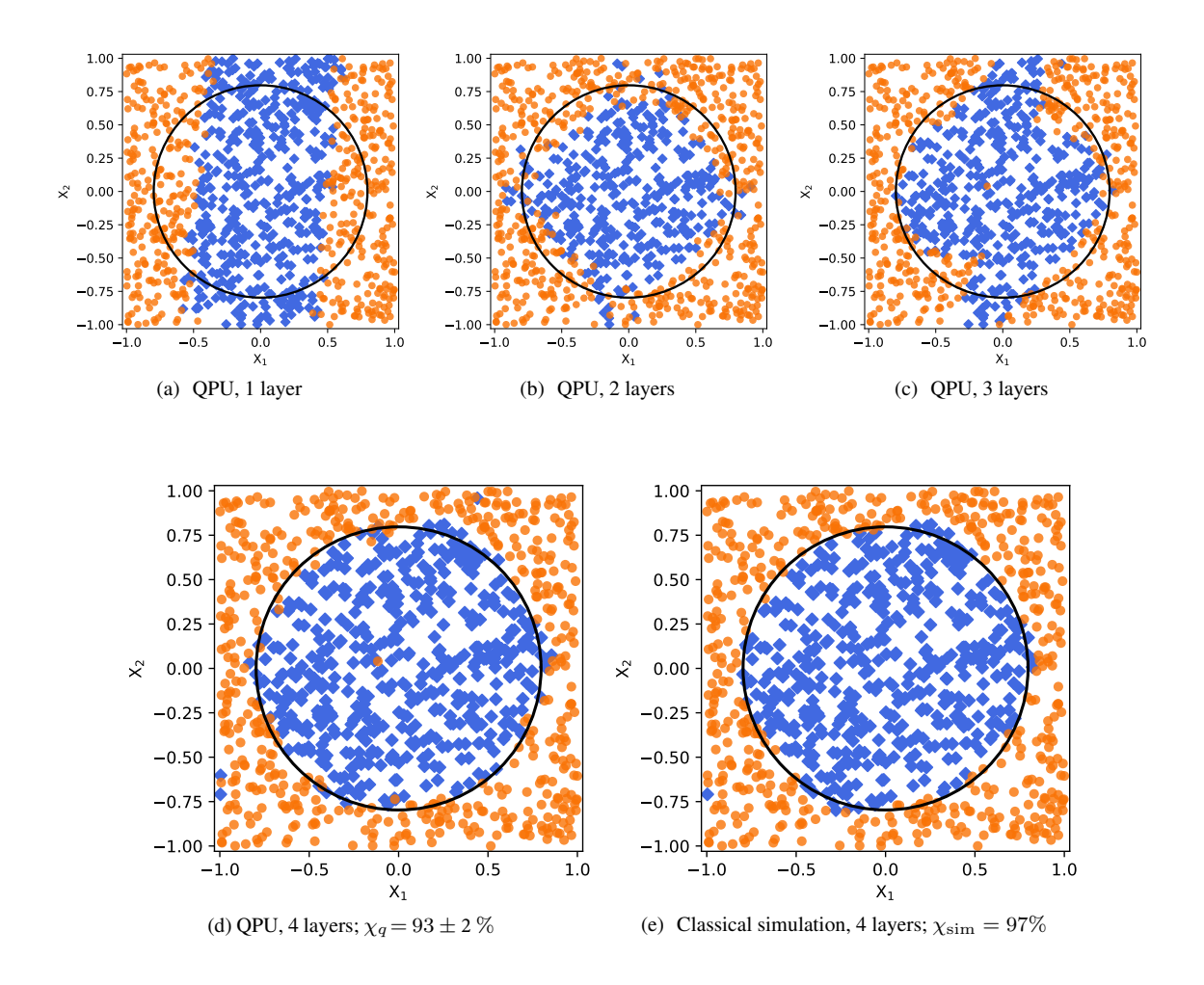


FIG. 2. Classifier test results. The ion trap based QPU classifier performed on 1000 random data points tests depicted in blue for points within and orange outside the boundary separating the circular feature shown in solid line. The depth of the circuit is increased by one, starting from 1-layer in (a) to 4 in (d). The result of the 4-layer QPU classifier (d) is compared with the same 4-layer simulator (e). Notice that the border between classes in the experimental results is not as sharply defined as in the simulated classification. This difference is due to the uncertainty of the quantum measurements and systematic errors.

 $\theta^q = \theta^{\text{sim}} + \delta\theta$. The experimental optimization is carried by scanning the parameter space in the vicinity of θ^{sim} and retrieving the configuration θ^q with best accuracy \mathcal{A}^q . We label the run of these improved parameters on the device as QPU(θ^q). This second step is currently available for quantum devices only if the loss function in the parameter space near the vicinity of the minimum is shallow and large deviations from the optimal parameters translate into small changes in the loss functions. In general, parameters for simulation and experiment do not exactly match each other. The difference may stem from the experimental inaccuracy when implementing optimal angles and occasional loss of information due to collisions with background molecules. This mismatch is seen in the parameters, but corrected in the final result thanks to the second optimization step. The full scan of the space of parameters is very time expensive in the present experiments. We shall only produce results for this higher level optimization in only two cases and defer a full analysis to a separate publication. We start by studying the simpler classification problem, a binary classification of 2D data samples, and use it to perform initial benchmark

of the quantum optimization step implemented on our machine. For every instance, we compare the accuracy of the simulated and the experimental classifiers \mathcal{A}^* and \mathcal{A}^{sim} , respectively. We include also its benchmarking against classical algorithms. In two cases, we have carried out the improvement step \mathcal{A}^q . We include images for few examples to illustrate some of the results. Additional images can be found in the Supplementary section of the present work for easy readability.

Two dimensional binary classification. A binary classifier is designed to learn the difference between patterns belonging to two classes, namely class 0 and 1; thereafter properly generalize that distinguishability to unlearned data. In this case, the dataset is represented by points on a plane, and the classes are defined as both sides of a curve acting as a boundary.

The first example of a binary classification problem corresponds to sorting points inside and outside a circle on the plane. The circle is centered at the middle of the plane and has half the total area (not a necessity), so that the instances belonging to the two classes are balanced. A random classifier would only guess 50% of test data properly. Fig. 2 shows experimental results for this classification problem for an increasing number of layers, and a comparison between the test data as classified by the QPU and an ideal classical qubit simulator. Here, each data point is depicted by its coordinates (x_1, x_2) and coloured according to its binary classification, namely blue for inside and orange for outside the circle, shown as a black solid line.

Fig. 2 shows the gradual improvement of classification as more layers are added. For 4 layers, the maximum layer number we used, the classification accuracy for the QPU is $\mathcal{A}^{sim}=93\pm2\%$, slightly lower than its classically simulated counterpart $\mathcal{A}^*=97\%$. The error here refers to the standard deviation of 10 repeated trials performed on the same dataset and it implies that underlying systematic uncertainty leads to an uncertainty of the accuracy. This confirms experimentally the expected behavior of a re-uploading scheme, namely the classifier is more accurate as more layer are added to the quantum circuit.

Let us note a difference in the behavior of both simulated and quantum classifiers. In the simulation, Fig. 2(e), the guessed boundary between classes is sharply defined, even though the guesses do not match exactly the data and the circle is slightly deformed. The results on the experimental data show uncertainty in the determination of data. See for instance the higher part of the circle. There are several points guessed to belong to different classes interspersed in a small area. The origin of this phenomenon is the inherent sampling uncertainty of the quantum device.

In this example, we also provide results for the experimental second optimization step. Figs. 3(a) show the land-scape of the accuracy for a specific subset of parameters in the vicinity of the optimum point as provided by the classical simulation. Due to the shallowness of the accuracy landscape in the parameter space, only three parameters effectively contribute to the final result, and thus the cost of searching optimal experimental configurations using a scanning technique is manageable. The plot shows that the optimal parameters for the experimental device deviates from that obtained by the estimate from the classical simulator. In addition to the landscape, the error in classification is also depicted in Fig. 3(b). The experimental errors are estimated separately, see Sec. *Methods*. Upon correction, the deviation between \mathcal{A}^q and \mathcal{A}^* nearly vanishes within the experimental uncertainty. After optimization, we obtain an improvement by more than 5% that brings accuracy of QPU to be as good as the simulator. This is better understood, by looking at the optimized error in figure 3(b) with respect to the simulation plotted as a function of the number of layers in the supervised learning process. In a realistic situation, the loss of information due to collision (small percentage to the systematic) can also be corrected by the observation of the emitted light level at the cost of longer operation time.

We also show the results for a pair of two-dimensional binary classification problems, namely *non-convex* and *crown*, as depicted in Fig. S1 in Supplementary section for 4 layers. In this case, the final accuracies for the QPU and the simulator $(A^{\text{sim}}) / (A^*)$ are *non-convex*:(92%) / (95%); *crown*: (87%) / (92%). In both cases, classes are defined in such a way that each one fills half the total feature space. Notice that these classification problems are harder than the circle discussed above [42]. The non-convexity feature of the first one makes it a more difficult for classification. In the *crown* case, the different classes are non-convex and, in addition, the in-out class is disjoint, making the problem even harder. Nevertheless, the final result shows that all problems can be solved in our QPU.

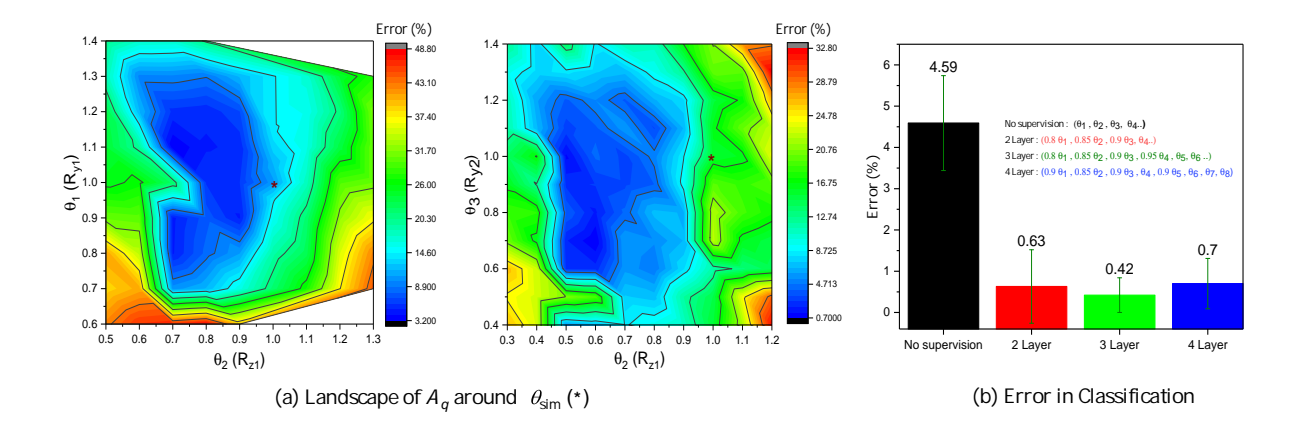


FIG. 3. Experimental optimization: The ion trap based QPU classifier used for binary classification of data within or outside a bounded circle is trained by varying the training parameters (θ_1 , θ_2 , θ_3 ,...) in the vicinity of the parameters obtained from the simulated training. The error surface plotted in color-coded surface plot in (a) shows the deviation of the optimal parameters from the trained minimum(\star). These plots are for 2-layer QPU and corresponds to Fig. 2(b). Similar training performed on the QPU leads to the betterment of the accuracy in the 3 and 4 layer QPU as shown in (b). Fig. (b) shows the error in classification is about 5% when simulated optimal parameters (θ_1 , θ_2 ,...) are used. On the contrary, when the parameters, after QPU optimization in the direct vicinity of the simulated parameters as in Fig. (a), are used for classification, it leads to a reduction in error below 1%. The values of the parameters, optimized by the QPU vary for different layers as shown in Fig. (b), improvement in the first two layers being most prominent.

Higher dimensional classification. It may appear that a single qubit QPU is capable of classifying features only in two dimensions. However, it is possible to encode the higher dimensional data into more than one layer, see Eq. (8) in Sec. Methods.

In order to test a classification performance for high-dimensional data, we extend the 2D-circle problem to 3D-sphere and 4D-hypersphere problems. The statement of the problem is equivalent and only the radius of the boundary is modified to accommodate the requirement that every class corresponds to half the feature space.

Results for the *hypersphere* classification are depicted in Fig. S2 in Supplementary section. To represent such a higher dimensional feature map we exploited the spherical symmetry of the feature and expressed the features in terms of the probability to distinguish one class from the other. In the histograms, the colors represent the class guessed by the classifier, while "Radius" stands for the location of the sample point. The y axis corresponds to the relative number of appearances. The vertical black line is located at the boundary between both classes. Therefore, the overlap region is the failure rate of the classifier to distinguish between the two classes without ambiguity. Our results show that we are able to classify the data as well as the simulator does. As in the *circle* example, the parameter set inherited from classical simulation implies a high error rate. This error can be further reduced from $\sim 13\%$ to $\sim 2\%$ after the experimental optimization step is performed, see Fig. S2(c) in the Supplementary section. Equivalent results for the *sphere* problem are recovered in the summary from Tab. I.

Multi-class classification. The single qubit QPU can also maximally separate three, four or more different classes [30]. To prove it experimentally, we provide an example of a three-class classification, *tricrown*, and three different examples of a four-classes problem, namely, 3 circles, squares and waves, in a 2D feature space. The results for all examples are depicted in Fig. 4 and in Fig. S3 in the Supplementary section for 4 layers for QPU and classical simulator. Results are respectively: tricrown: (95%) / (91%); 3 circles:(85%) / (90%); squares:(93%) / (97%); waves:(90%) / (94%).

These datasets present different hardness for classification [42]. For the *tricrown* example, the difficulty is to add a third class to the *crown* problem. This, however, makes all regions in the feature space joint. The 3 *circles*

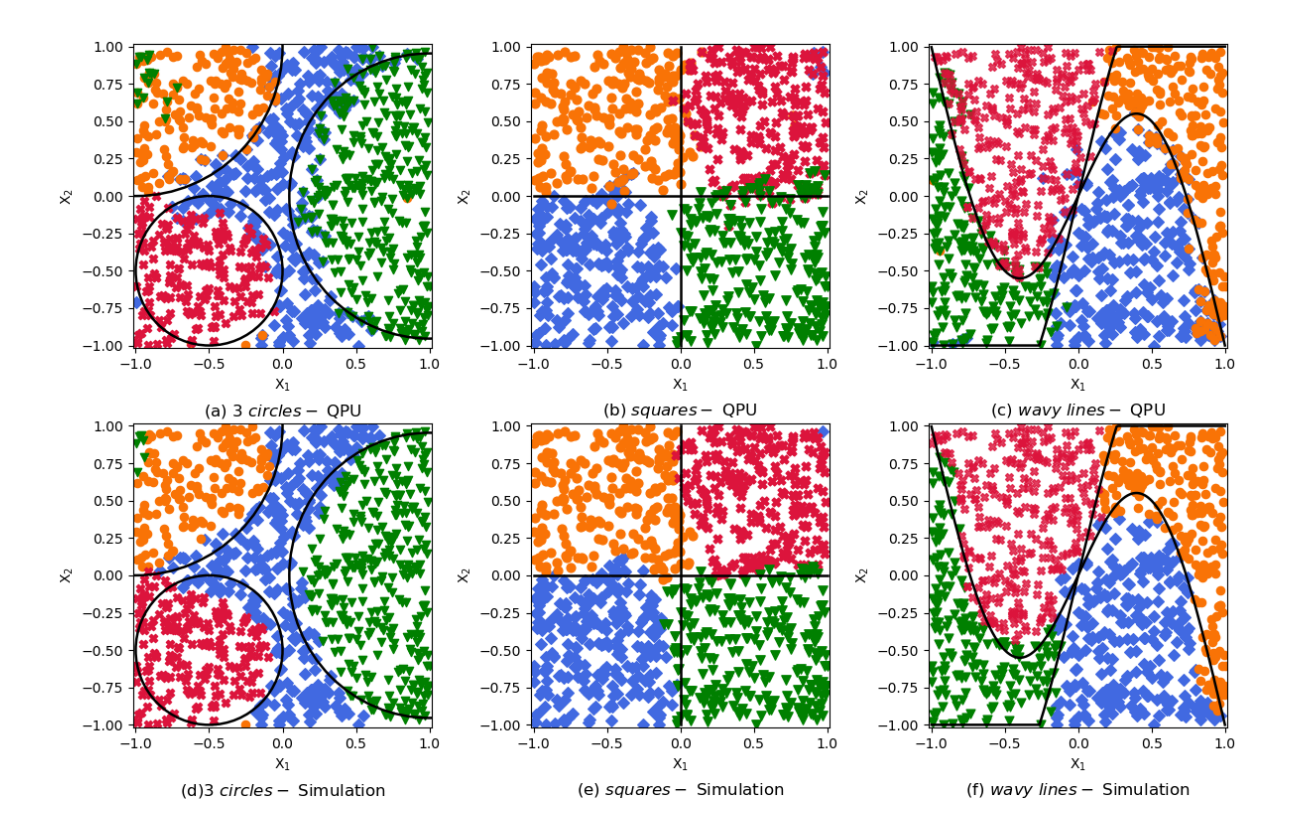


FIG. 4. Multi-class classification. The columns show, from left to right, 3 circles, squares and wavy lines problems. The top row corresponds to experimental QPU results, while the bottom row corresponds to classical simulations. Results include 1000 random data points, the classes are depicted in different colors and symbols, and the boundaries are defined by solid black lines. Notice that the border between classes in the experimental results is not sharply defined, unlike in the simulated classification. This difference is due to the uncertainty of the quantum measurements.

feature is composed of 3 different and separated classes, that is the circles, and a fourth class filling the space in between. Thus, the classifier is forced to separate the space corresponding to different classes. In the *squares* case, all classes are equivalent and connected to each other. That forces the classifier to be flexible enough as to map close points to very different areas of the Hilbert space. For *waves*, the difficulty of non-convex datasets is added. The experimental classifier succeed in solving all those problems.

Table I presents a summary of the accuracies obtained by the experimental quantum classifier as compared to the simulated results serving as the starting point for the experimental optimization. Each problem was solved using an independent Ansatz (A, B) specified in the table, see Sec. *Methods* for further details. We also benchmark the quantum results against classical models whose complexity is comparable. To be precise, we have considered a single-hidden-layer neural network and a support vector machine classifier. In the case of Neural Networks, several activation functions were tested for every problem, and the result depicted in Tab. I is the most accurate one. The number of neurons in the hidden layer is chosen to match the number of parameters in the quantum classifier. In the case of support vector machine classifier, different kernels are used, and again the best result is retrieved. Notice that, in this case, it is not possible to tune the number of parameters available to carry the classification since they depend on the size of the training set. This model is however shown for completeness. In all classical cases, the computations were done using the scikit-learn python package [43] and following pre-defined models.

In light of these results it is possible to see that the performance of the quantum classifier is comparable to that

Problem (# classes)		Classical algorithms		Quantum re-uploading			Ansatz
		Neural Network	Support Vector Machine	Simulation	$QPU(\boldsymbol{\theta}^{\mathrm{sim}})$	$QPU(\boldsymbol{\theta}^{\mathrm{q}})$	Alisatz
Circle	(2)	0.98	0.96	0.97	0.93	0.96	A
Crown	(2)	0.71	0.82	0.92	0.87		В
Non-Convex	(2)	0.98	0.79	0.95	0.92		В
Sphere	(2)	0.95	0.91	0.74	0.66		A
Hypersphere	(2)	0.76	0.92	0.75	0.64	0.73	A
Tricrown	(3)	0.97	0.83	0.95	0.91		A
3 circles	(4)	0.93	0.92	0.90	0.85		В
Squares	(4)	0.99	0.95	0.97	0.93		A
Wavy Lines	(4)	0.99	0.89	0.94	0.90		A

TABLE I. Comparison between single-qubit re-uploading quantum classifier and two well-known classical classification techniques, namely single-hidden-layer neural networks and support vector machines. The experimental data and its simulated analogue is provided here with 4 Layer and 100 repetitions on the quantum part, and its equivalent in complexity for the neural network. The uncertainty of experimental data is $\pm 2\%$. The error refers to the standard deviation of 10 repeated trials performed on the same dataset and it implies that underlying systematic uncertainty leads to an uncertainty of the accuracy (see Sec. *Methods* for further details). Only two cases have been further optimized using an exploration done only with the quantum device.

of classifiers when the training dataset has a low feature dimension. On the contrary, when datasets with more features are considered, the performance degrades but still comparable to simulated results. This limitation can be addressed by increasing the flexibility of the model, as it was shown in Ref. [30]. Two ways to achieve higher flexibility is to either add more layers to the quantum classifier or to change the encoding scheme to one with more degrees of freedom. However, the most relevant outcome of this comparison is that in a setting where the number of gates are restricted, a quantum classifier shown here outperforms a classical neural network. This quantum advantage of our approach scales as the number of required nodes in the neural network [44]. As shown here, the accuracy of the quantum classifier improves with the depth of the circuit which is equivalent to the number of nodes in a neural network.

DISCUSSION

We have experimentally implemented a quantum supervised classifier on a QPU. The QPU is based on an ion trap platform, which is known for high fidelity gates [35, 39, 45]. This high fidelity allows to implement a quantum classifier based on the recently proposed re-uploading algorithm [29, 30]. To the best of our knowledge, the experiment reported here, is the first implementation of problems of this kind in the NISQ era with limited qubit number that shows a definitive advantage on the number of physical gates required when compared to classical approaches.

To enhance the performance of the algorithm, the classifier is trained in two steps, first using a classical simulator, and then at the gate level of the quantum device. This second step permits to mitigate possible systematic errors from the quantum device. With this method, the accuracy of the classifier on the quantum experiment is enhanced up to 5-10% depending on the problem. The resultant high performance of the QPU allowed comparable outcome to that of a classical simulator and classical classifiers of equivalent complexity in the number of parameters used.

The examples of the datasets provided here include rudimentary but non-trivial classification tasks that were successfully solved, including binary, multi-class and high dimensional datasets. To complete the bench-marking, we showed that our QPU can not only classify multi-class and higher dimensional feature maps but also shows competing results in classifying non-convex and linear feature maps. Both experimental and simulated results are benchmarked against well-established classical methods. The performances for quantum and classical cases are comparable, see Tab. I.

Other approaches explore the possibilities to classify complex datasets by implementing a variety of quantum

models. The aim of those models is to compare their performance with classical procedures of similar complexities. However, this work demonstrates experimentally that a minimalistic quantum system, namely a single qubit, is capable to perform non-trivial classification tasks. Following the work of Refs. [29–31], this work constitutes the first experimental proof, as related to the re-uploading scheme may become part of OML strategies.

METHODS

Experimental setup. The QPU described here, is based on a ¹³⁸Ba⁺ ion trapped and laser cooled in a linear blade trap [35, 36, 46]. The qubit is well-characterized in terms of both its internal [36] and external states [47]. The main upgrade with respect to our previous setup lies in the hardware to better control the qubit phase. In addition, we modified the control software to implement quantum algorithms requiring long circuit depth with low latency. The qubit is formed between the electronic ground state $S_{\frac{1}{2},-\frac{1}{2}}$ and the excited state $D_{\frac{5}{2},-\frac{1}{2}}$ which are coupled only by the E2 transition, requiring ultra-low linewidth laser at 1762 nm wavelength. The laser is phase locked to a ultra-low expansion (ULE) cavity achieving an estimated linewidth of ≤ 100 Hz (estimated from the measured atomic resonance). Prior to performing each algorithmic cycle the qubit is first Doppler cooled to the Lamb-Dicke regime [36] via a fast dipole transition (between S-P levels) at 493 nm and a re-pump laser (between D-P levels) at 650 nm. In this regime the internal and external states of the qubit are decoupled and hence single qubit gate errors are not influenced by the motion of the qubit. Subsequently, the qubit is initialized to the state $|0\rangle \equiv \left|S_{\frac{1}{2},-\frac{1}{2}}\right>$ by optical pumping [48], achieved by selectively de-populating the other ground state $S_{\frac{1}{3},+\frac{1}{3}}$ using a σ^{-} polarized laser beam at 493 nm propagating along the quantization axis (externally applied magnetic field B direction). The strength and direction of the B field is optimized to achieve high fidelity state initialization of > 99% within an optical pumping time of $< 50\mu$ s only. The resultant strength of the magnetic field corresponds to a ground state Zeeman splitting of about 2 MHz. Once the qubit is initialized, any single qubit rotational gate is implemented by resonantly driving the qubit with full control over the laser phase, power and laser on-time. A direct digital synthesizer (DDS) based on AD9959 chip is used to control the phase, frequency and power of the laser as the sequential gates are applied on the qubit. The DDS is disciplined by a rubidium frequency standard (SRS FS725), eliminating the long term frequency drift of the DDS clock, thus maintaining the phase relations of the sequential gates of the classifier. As classical data is uploaded in-the-fly, the latency of uploading the DDS parameters play a crucial role. The latency is minimized by pre-loading the full sequence of the phase, frequency and power data to an on-chip memory of the DDS. The DDS output is then controlled by an external trigger generated from a Field Programmable Gate Array (FPGA) based pulse pattern generator (PPG) that controls the time sequence of the entire experiment. In separate experiments we optimized and quantified the single qubit gate errors by performing randomized benchmarking [35], in addition to minimizing the errors due to initialization (state preparation) as well as state detection. The optimized setup is then used for the implementing the data re-uploading algorithm as described in the following.

Experimental procedure. Each data point shown in Figure 2 or any of the other classifier plots, comprises of 100 repeat experiments. Every experiment, consists of a sequence of operations performed on the qubit as shown in figure (6). The qubit is initialized in two operational steps: the 138 Ba $^+$ ion is first laser cooled by driving the $S_{1/2}$ - $P_{1/2}$ cyclic transition and followed by the optical pumping of the ion to $S_{1/2,-1/2} \equiv |0\rangle$ state using a σ -polarized light resonant to $S_{1/2,1/2}$ - $P_{1/2,-1/2}$ transition. Once initialized to the $|0\rangle$ state, the qubit is ready for single qubit gates operations. The classical dataset comprised of coordinates of points in a plane, are converted to rotation angles following the anzats as in eq. (7,8). Depending on the data to be uploaded, single qubit gates are implemented by resonantly driving the qubit transition between $S_{1/2,-1/2}$ - $D_{5/2,-1/2}$ with well-controlled phase and operation time, while the frequency and power of the laser are kept constant. An AOM controls the phase and frequency of the 1760 nm laser implementing the rotation gates. The phase of the AOM is directly controlled by a DDS which supplies the RF signal to the AOM via an amplifier. The laser-qubit interaction time sets the rotation angle θ ; it is controlled by a RF switch that implements pulse-shaping thus reducing off-resonant phase noise in

the circuit. Therefore, we have direct and precise control over the axis and angle of rotations. The sequence for a typical 4-layer implementation is composed of the following gates: $R(\pi/2, \theta_1)$, $R(\theta_2, \theta_3)$, $R(\theta_4, \theta_5)$, $R(\theta_6, \theta_7)$, $R(\theta_8, 0)$, where $R(\phi, \theta)$ is defined as:

$$R(\phi, \theta) = \begin{bmatrix} \cos\frac{\theta}{2} & -ie^{-i\phi}\sin\frac{\theta}{2} \\ -ie^{i\phi}\sin\frac{\theta}{2} & \cos\frac{\theta}{2} \end{bmatrix}$$
 (6)

The time sequence shown in fig. (6), is controlled by a FPGA with a time jitter below 10 ns. The current version of the DDS controlling the phase of the laser is limited by the on-chip memory to 16 phase modulation steps thus limiting the layers to six, which is sufficient for the current discussion. Once the circuit runs over all the layers, the wavefunction overlap of the final state of the qubit on to the label state is measured. In case of binary classification, the final state is projected on to the label state $|0\rangle$ and the overlap is measured by observing spontaneously emitted photons while the qubit is excited by 493 nm laser. With a photon collection time of 2 ms, the qubit state is determined by choosing a photon-count threshold of 15 counts/2 ms such that the bright state is clearly discriminated from the dark state. This projective measurement is 100\% efficient in discriminating the qubit state $S_{1/2}$ (bright) and $D_{5/2}$ (dark). Taking repeated measurements on the same state provides the probability and hence the projection of the state along the σ_z -axis. In general, for any classification problem with more than two classes, the label states for each class is pre-defined by choice. Therefore, instead of measuring the final state of the circuit, the final state is projected to the label state and the overlap is measured along the three rotational axis of the qubit. This requires additional two rotations before performing state discrimination. The overlap, a value between 0 (no overlap) and 1 (full overlap), for each data point based on a threshold is designated a success (1) or failure (0) to be within a class. The points designated as success are plotted in all the classification figures shown in this article with different colours denoting the different classes.

Data analysis and source of error. The accuracy of the data re-uploading algorithm primarily relies on the the fidelity of individual single qubit rotation gate. The gate, as explained earlier, is operated by controlling the laser phase and interaction time, while keeping the intensity at the ion position and the frequency of the laser constant. Therefore, the residual error in the gate operation is reflected in the accuracy of the classifier as define in eq. (5). In eq. (6), the rotation angles $\phi = (\Delta/\hbar)t_{op} + \delta\phi$ and $\theta = (\Omega/\hbar)t_{op}$, where Δ is the laser detuning, t_{op} is the operation time of gates, Ω' is the modified Rabi frequency and $\delta\phi$ is the relative phase of the laser with respect to the qubit. The modified Rabi frequency $\Omega' = \sqrt{\Omega_0^2 + \Delta^2}$ with Ω_0 denoting the resonant Rabi frequency. Furthermore, the resonant Rabi frequency is proportional to the square root of the intensity, I_0 , at the ion position. Therefore each of the independent variables $\delta\phi$, t_{op} , Δ and I_0 contributes to the error in a rotation gate, thus influencing the accuracy of the quantum data re-upload classifier. We have characterized these factor separately using the *circle* classification problem as a test-bed. The errors shown in fig. (5) are obtained as inaccuracy percentage of classification as compared to the simulation results. In the following, we will discuss in detail the influence of each of these parameters on the accuracy of the classifier:

- 1. **Phase:** The DDS controls the RF phase of the AOM which determines the relative phase of the laser. Each DDS is synchronized to a rubidium atomic clock which is accurate to one part in 10^{10} and thus contributes negligibly to the phase error. The DDS is however triggered by the FPGA which has time jitter below 10 ns leading to phase noise on the qubit below 0.1% for a Rabi π time of $12~\mu s$.
- 2. Interaction time: The laser-qubit interaction time is determined by the FPGA which is precise to 1 ns. Therefore the contribution to the accuracy of the classifier is less than 0.01%. However, due to the time jitter below 10 ns, its contribution to the accuracy is below 0.1%. Occasional collision with the residual background gas molecule during the interaction time leads to a projection to the state $|0\rangle$, thus losing the final state information and hence error in the classification. Usually this error becomes smaller with larger statistics.
- 3. Laser-qubit detuning: The detuning of the laser with respect to the qubit frequency denoted by Δ modifies the Rabi frequency. In order to quantify the influence of any unwanted fluctuations of the detuning on the

classifier accuracy, we first quantified the range of Rabi frequency fluctuation within the experimental time of about 10 min. However, to ensure that our classifier accuracy is limited by systematic errors not by statistical, we measured the statistical error in the classification problem by repeating the experiment for each data point between 25 to 1000 times (see fig. (5a)). The error (or in-accuracy) decreases from 12% to about 4% for 100 repetitions and then stay nearly the same, limited by systematic. The fluctuation of the laser frequency with respect to the atomic resonance is captured over a time period of 20 min (twice the duration of an experiment) as plotted in fig. (5b). The random variation of the Rabi frequency over time is mostly caused by the magnetic field noise as we have separately measured the laser frequency drift to be $\leq 5 \text{ kHz}/24 \text{ hrs } [35]$. To minimize the impact of the residual magnetic field noise, we use electronic levels ($\Delta m = 0$) that are weakly sensitive to such noise. In addition, the detuning also indirectly influence the modified Rabi frequency. To check its influence, we varied the Rabi frequency, shown in Fig. 5(c), by varying the detuning within a 2 kHz range (as expected from the fig. (5b)). The result shows below 5% accuracy for the classifier when operating for 10 min.

4. Laser intensity: The Rabi frequency is fixed by setting the power and frequency of the laser at the start of the experiment. Any change in the Rabi frequency during the experiment, therefore leads to error in applied qubit rotation angle. Therefore, the accuracy of the classifier, depends on the Rabi frequency fluctuations due to intensity fluctuation apart from detuning as discussed earlier. The intensity is influenced by two factors namely: (a) laser power noise and (b) laser beam pointing error. In our experiment, the laser beam is tightly focused on the ion by a high Numerical Aperture (NA~0.4) in-vacuum lens. To obtain high intensity at the ion position, the light is focused tightly to about 10μm beam waist. In order to capture the influence of laser power variations on the classification error, we varied power (plotted in terms of modified Rabi frequency) in fig. (5d). Thus it is seen that the influence of intensity noise accounts to 5% error in accuracy. Thus, to avoid the influence of Rabi frequency fluctuation within the experimental time of ~ 10 min, we reduce the Rabi frequency from 312 kHz to 40 kHz such that the absolute error also reduces. This leads to an overall error of only 2% on the classifier output.

Re-uploading classifier. Quantum circuits and classical neural networks can be used as data processing machines for classification. Neural networks are often structured as feed-forward architectures where initial data are introduced several times into a first hidden layer, and then are processed subsequently layer by layer. A quantum circuit of a single qubit seems to be at disadvantage as the initial data can enter in the first neuron and then is processed by one gate. The complexity of neural networks multi-processing seems to be lost in a single qubit quantum circuit. The way out to this problem is to re-upload data on subsequent single qubit gates circuit [30, 31].

The re-uploading strategy works as follows. Data are incorporated on a single qubit in an unbiased manner, that is using at most a linear transformation $\vec{x} \to \vec{w} \cdot \vec{x} + b$, where \vec{x} represent the variables of a given pattern and \vec{w} and b are circuit parameters to be trained. The non-linear processing of this entry is done by the quantum laws of nature, that is by the unitary exponential single qubit gate. Then, subsequent gates act similarly, each one adding more degrees of freedom to the quantum circuit. A final measurement is used to compute a cost function to be minimized by choosing appropriate parameters for the gates.

Re-uploading has proven successful. It has also been understood as a mean to create a universal approximant with a single qubit [29]. Indeed, a series of single-qubit quantum gates can approximate any function point-by-point, as it can be proven to reproduce a Fourier series. However, the complexity that is achievable for circuits with many qubits and gates remains veiled yet.

Nearly all QML algorithms perform three essential tasks: (a) loading of classical data into the quantum processor, (b) processing of the quantum data and (c) measurement of the final quantum state. However, data re-uploading consists of only two steps since loading and processing of data are carried out simultaneously through the circuit. This difference is feasible because the data is encoded into the rotation angle of gates shaping the quantum circuit, together with some tunable parameters. To do so, the circuit is composed of several consecutive layers depending both on data and some tunable parameters. In addition, each layer is built with two or more non-commuting rotational gates.

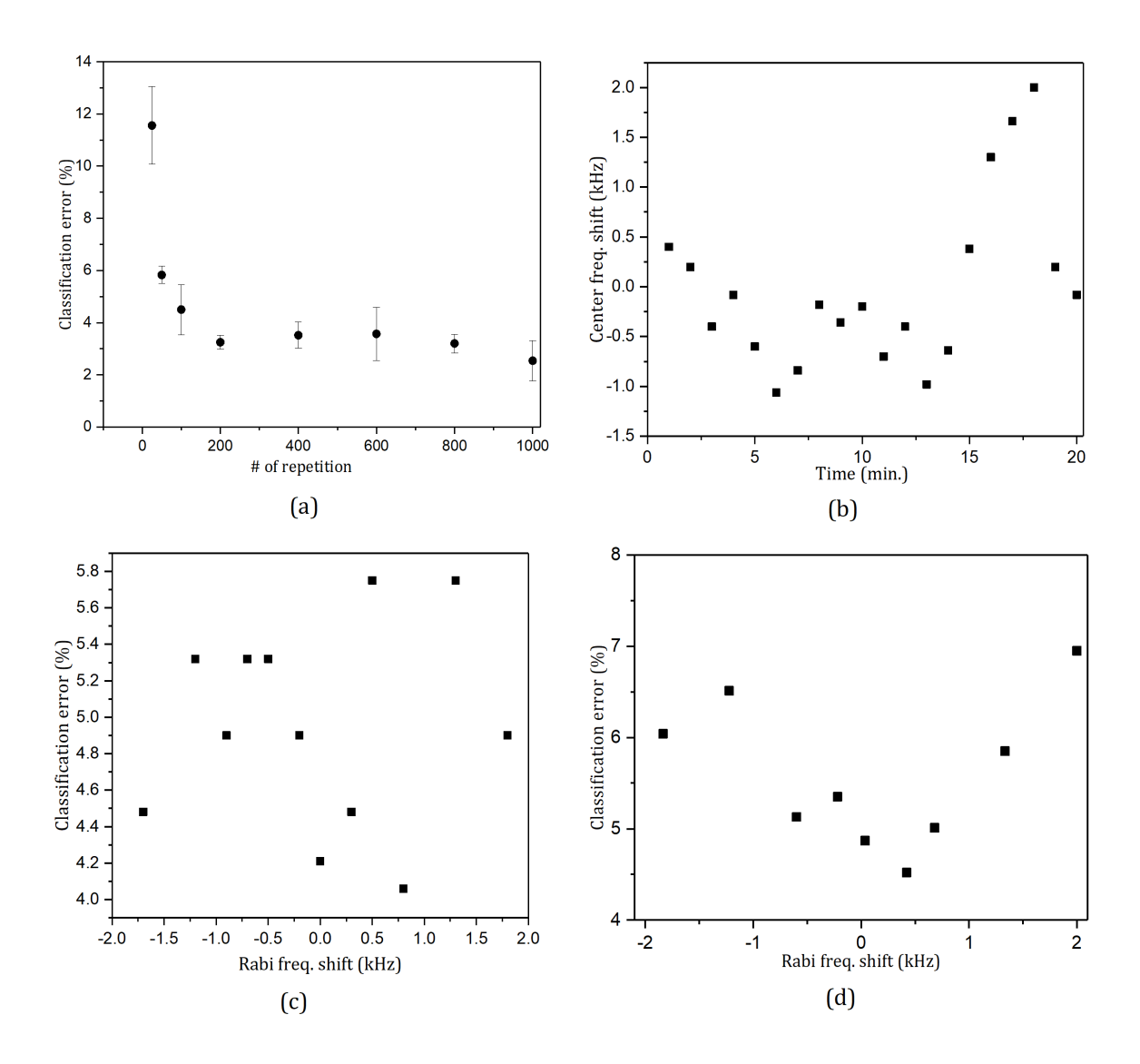


FIG. 5. Systematic error analysis: All the results shown here are related to the binary classification of circle as in fig. (2). The errors are classification error. (a) The classifier error as a function of the number of repeated experiments. The error bar at each point corresponds to 1 standard deviation of a number of repeat measurements for same number of repeated experiments under the same condition. The exact number of repeat measurements varies between 5 and 10. (b) Variation of the resonance frequency as a function of time. The range of Rabi frequency fluctuation within a typical experimental time of ≤ 10 min. is about 2 kHz. (c) Error in binary classification of a circle feature with the variation of laser frequency detuning measured in terms of the Rabi frequency. The variation in the value of classification error is about 2% within the experimental time of ~ 10 min. (d) The same plot as in (c) but by varying the laser power measured in terms of the Rabi frequency.

A cornerstone for having a successful model is the choice of a set of label states $\{|\phi_y\rangle\}$, see Eq. (2). This set must be maximally orthogonal to increase distinguishability. In the case of binary classification, two completely orthogonal basis states exist, returning an optimal configuration. For more complex classification tasks, finding the set of maximally orthogonal states is a problem on its own. For the particular case of 3 and 4 classes, the solutions

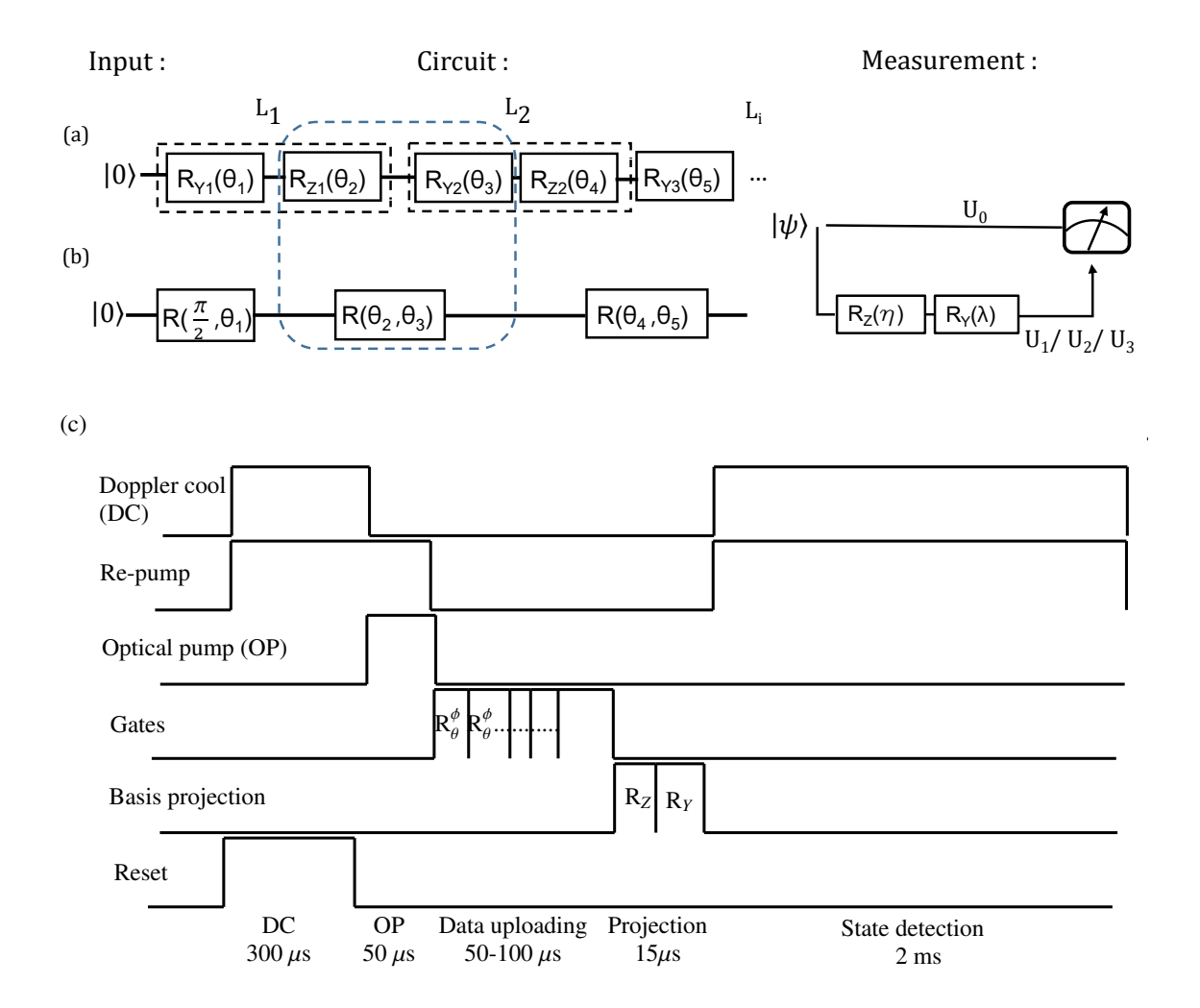


FIG. 6. Experimental implementation of quantum classifier circuit: (a) The algorithm to implement quantum classifier represented by layers (L_i) of two non-commuting rotational gates. (b) In the experiment R_z and R_y gates are concatenated into one rotational gate $(R(\phi,\theta)\equiv R_\theta^\phi)$ with modified rotation axis. For one qubit it is possible to define at most two orthogonal states, so unitary operation U_0 works only for a binary classification whereas for multi-class classifications a set of unitary operations $(U_i\equiv R_z(\eta)R_y(\lambda))$ are used to define other label states(see text for more details).(c) The time sequence used in the experiment to perform each classifier measurement.

correspond to a regular triangle on any equatorial plane and a tetrahedron respectively, see Ref. [30] for further details.

Circuit definitions: We propose two different explicit Ansätze for the circuit defined in Eq. (1). Ansatz A is

$$U_A(\vec{x}, \vec{\theta}) = R_z(\varphi) R_y(\vec{w} \cdot \vec{x} + b). \tag{7}$$

where \vec{x} is a point from training data, and R_z and R_y are single-qubit rotations around the z and y axis respectively. The set of training data is denoted as $\mathbb{D} = \{(\vec{x}, y)\}$, where j is the class to which \vec{x} belongs. Note that this ansatz does not have any constraint in the dimensionality of \vec{x} since any data can be easily accommodated by increasing

the dimension of \vec{w} . Thus, it can be used for any dataset. Notice that in this circuit only rotations around the Y axes gets the data introduced, while rotations around Z are required to create non-linearities in the circuit [29].

Ansatz B holds only for 2-dimensional datasets and it is defined as

$$U_B(\vec{x}, \vec{\theta}) = R_z(w_2 x_2 + b_2) R_y(w_1 x_1 + b_1). \tag{8}$$

This ansatz introduces data in all rotation gates and non-linearities are expected to arise faster from the interaction of different features of \vec{x} [30].

ACKNOWLEDGMENTS

This research is supported by the Quantum Engineering Program under National Research Foundation (Award No. QEP-P6) and CQT Core grant. A.P.-S. acknowledges financial support from Secretaria d'Universitats i Recerca del Departament d'Empresa i Coneixement de la Generalitat de Catalunya, co-funded by the European Union Regional Development Fund within the ERDF Operational Program of Catalunya (project QuantumCat, ref. 001-P-001644).

- * cqttaru@nus.edu.sg
- † manas.mukh@gmail.com
- E. Bernstein and U. Vazirani, Quantum complexity theory, SIAM Journal on Computing 26, 1411 (1997), https://doi.org/10.1137/S0097539796300921.
- [2] P. W. Shor, Algorithms for quantum computation: discrete logarithms and factoring, in *Proceedings 35th Annual Symposium on Foundations of Computer Science* (1994) pp. 124–134.
- [3] L. M. K. Vandersypen, M. Steffen, G. Breyta, C. S. Yannoni, M. H. Sherwood, and I. L. Chuang, Experimental realization of shor's quantum factoring algorithm using nuclear magnetic resonance, Nature 414, 883 (2001).
- [4] S. Debnath, N. M. Linke, C. Figgatt, K. A. Landsman, K. Wright, and C. Monroe, Demonstration of a small programmable quantum computer with atomic qubits, Nature **536**, 63 (2016).
- [5] D. Maslov, J.-S. Kim, S. Bravyi, T. J. Yoder, and S. Sheldon, Quantum advantage for computations with limited space, Nature Physics 10.1038/s41567-021-01271-7 (2021).
- [6] F. Arute, K. Arya, J. M. Martinis, et al., Quantum supremacy using a programmable superconducting processor, Nature 574, 505 (2019).
- [7] H.-S. Zhong, H. Wang, Y.-H. Deng, M.-C. Chen, L.-C. Peng, Y.-H. Luo, J. Qin, D. Wu, X. Ding, Y. Hu, and et al., Quantum computational advantage using photons, Science 370, 1460–1463 (2020).
- [8] Y. Wu, W.-S. Bao, S. Cao, F. Chen, M.-C. Chen, X. Chen, T.-H. Chung, H. Deng, Y. Du, D. Fan, and et al., Strong quantum computational advantage using a superconducting quantum processor, Physical Review Letters 127, 10.1103/phys-revlett.127.180501 (2021).
- [9] C. Cortes and V. Vapnik, Support-vector networks, Machine Learning 20, 273 (1995).
- [10] D. Saad, ed., On-Line Learning in Neural Networks (Cambridge University Press, USA, 1999).
- [11] C. M. Bishop, Neural networks and their applications, Review of Scientific Instruments 65, 1803 (1994), https://doi.org/10.1063/1.1144830.
- [12] S. Russell, Artificial intelligence: a modern approach (Prentice Hall, Upper Saddle River, New Jersey, 2010).
- [13] M. Mohri, Foundations of machine learning (MIT Press, Cambridge, MA, 2012).
- [14] Y. Liu, S. Arunachalam, and K. Temme, A rigorous and robust quantum speed-up in supervised machine learning (2020), arXiv:2010.02174 [quant-ph].
- [15] V. Dunjko and H. J. Briegel, Machine learning & artificial intelligence in the quantum domain: a review of recent progress, Reports on Progress in Physics 81, 074001 (2018).
- [16] M. Schuld, A. Bocharov, K. M. Svore, and N. Wiebe, Circuit-centric quantum classifiers, Physical Review A 101 (2020).
- [17] J. Biamonte, P. Wittek, N. Pancotti, P. Rebentrost, N. Wiebe, and S. Lloyd, Quantum machine learning, Nature 549, 195 (2017).

- [18] K. Bharti, A. Cervera-Lierta, T. H. Kyaw, T. Haug, S. Alperin-Lea, A. Anand, M. Degroote, H. Heimonen, J. S. Kottmann, T. Menke, W.-K. Mok, S. Sim, L.-C. Kwek, and A. Aspuru-Guzik, Noisy intermediate-scale quantum (NISQ) algorithms (2021), arXiv:2101.08448 [quant-ph].
- [19] J. Preskill, Quantum Computing in the NISQ era and beyond, Quantum 2, 79 (2018).
- [20] X.-D. Cai, D. Wu, Z.-E. Su, M.-C. Chen, X.-L. Wang, L. Li, N.-L. Liu, C.-Y. Lu, and J.-W. Pan, Entanglement-based machine learning on a quantum computer, Phys. Rev. Lett. 114, 110504 (2015).
- [21] P. Rebentrost, M. Mohseni, and S. Lloyd, Quantum support vector machine for big data classification, Phys. Rev. Lett. 113, 130503 (2014).
- [22] V. Havlíček, A. D. Córcoles, K. Temme, A. W. Harrow, A. Kandala, J. M. Chow, and J. M. Gambetta, Supervised learning with quantum-enhanced feature spaces, Nature 567, 209 (2019).
- [23] C. Hempel, J. M. T. M. Christine Maierand Jonathan Romero, H. Shen, P. Jurcevic, B. P. Lanyon, P. Love, R. Babbush, A. Aspuru-Guzik, R. Blatt, and C. F. Roos, Quantum chemistry calculations on a trapped-ion quantum simulator, Physical Review X 8, 031022.
- [24] S. Resch and U. R. Karpuzcu, Quantum computing: An overview across the system stack (2019), arXiv:1905.07240 [quant-ph].
- [25] C. Figgatt, D. Maslov, K. A. Landsman, N. M. Linke, S. Debnath, and C. Monroe, Complete 3-qubit grover search on a programmable quantum computer, Nature Communications 8, 10.1038/s41467-017-01904-7 (2017).
- [26] Y. Nam, J.-S. Chen, J. Kim, *et al.*, Ground-state energy estimation of the water molecule on a trapped-ion quantum computer, npj Quantum Information **6**, 10.1038/s41534-020-0259-3 (2020).
- [27] S. Johri, S. Debnath, A. Mocherla, A. Singh, A. Prakash, J. Kim, and I. Kerenidis, Nearest centroid classification on a trapped ion quantum computer (2020), arXiv:2012.04145 [quant-ph].
- [28] M. S. Rudolph, N. B. Toussaint, A. Katabarwa, S. Johri, B. Peropadre, and A. Perdomo-Ortiz, Generation of high-resolution handwritten digits with an ion-trap quantum computer (2020), arXiv:2012.03924 [quant-ph].
- [29] A. Pérez-Salinas, D. López-Núñez, A. García-Sáez, P. Forn-Díaz, and J. I. Latorre, One qubit as a universal approximant (2021), arXiv:2102.04032 [quant-ph].
- [30] A. Pérez-Salinas, A. Cervera-Lierta, E. Gil-Fuster, and J. I. Latorre, Data re-uploading for a universal quantum classifier, Quantum 4, 226 (2020).
- [31] M. Schuld, R. Sweke, and J. J. Meyer, The effect of data encoding on the expressive power of variational quantum machine learning models, Physical Review A 103, 032430 (2021), arXiv: 2008.08605.
- [32] K. R. Brown, A. C. Wilson, Y. Colombe, C. Ospelkaus, A. M. Meier, E. Knill, D. Leibfried, and D. J. Wineland, Single-qubit-gate error below 10⁻⁴ in a trapped ion, Phys. Rev. A 84, 030303 (2011).
- [33] P. Wang, C.-Y. Luan, M. Qiao, M. Um, J. Zhang, Y. Wang, X. Yuan, M. Gu, J. Zhang, and K. Kim, Single ion qubit with estimated coherence time exceeding one hour, *Nature Communications* 12, 233 (2021).
- [34] P. Easom-Mccaldin, A. Bouridane, A. Belatreche, and R. Jiang, On depth, robustness and performance using the data re-uploading single-qubit classifier, IEEE Access 9, 65127 (2021).
- [35] D. Yum, D. D. Munshi, T. Dutta, and M. Mukherjee, Optical barium ion qubit, J. Opt. Soc. Am. B 34, 1632 (2017).
- [36] T. Dutta and M. Mukherjee, A single atom noise probe operating beyond the heisenberg limit, npj Quantum Information 6, 3 (2020).
- [37] D. C. McKay, C. J. Wood, S. Sheldon, J. M. Chow, and J. M. Gambetta, Efficient z gates for quantum computing, Phys. Rev. A 96, 022330 (2017).
- [38] D. Maslov, Basic circuit compilation techniques for an ion-trap quantum machine, New Journal of Physics 19, 023035 (2017).
- [39] E. Knill, D. Leibfried, R. Reichle, J. Britton, R. B. Blakestad, J. D. Jost, C. Langer, R. Ozeri, S. Seidelin, and D. J. Wineland, Randomized benchmarking of quantum gates, Phys. Rev. A 77, 012307 (2008).
- [40] N. Hansen, The cma evolution strategy: A comparing review (2006).
- [41] R. Byrd, P. Lu, J. Nocedal, and C. Zhu, A limited memory algorithm for bound constrained optimization, SIAM J. Sci. Comput. 16, 1190 (1995).
- [42] T. K. Ho and M. Basu, Measuring the complexity of classification problems, in *Proceedings 15th International Conference on Pattern Recognition*. *ICPR-2000*, Vol. 2 (2000) pp. 43–47 vol.2.
- [43] F. Pedregosa, G. Varoquaux, E. Duchesnay, *et al.*, Scikit-learn: Machine learning in Python, Journal of Machine Learning Research **12**, 2825 (2011).
- [44] C.-H. Tsai, Y.-T. Chih, W. H. Wong, and C.-Y. Lee, A hardware-efficient sigmoid function with adjustable precision for a neural network system, IEEE Transactions on Circuits and Systems II: Express Briefs 62, 1073 (2015).
- [45] J. Gaebler, T. Tan, Y. Lin, Y. Wan, R. Bowler, A. Keith, S. Glancy, K. Coakley, E. Knill, D. Leibfried, and D. Wineland, High-fidelity universal gate set for ⁹Be⁺ ion qubits, Phys. Rev. Lett. 117, 060505 (2016).

- [46] T. Dutta, D. D. Munshi, D. Yum, R. Rebhi, and M. Mukherjee, An exacting transition probability measurement a direct test of atomic many-body theories, Scientific Reports 6, 29772 (2016).
- [47] N. Van Horne, D. Yum, T. Dutta, P. Hänggi, J. Gong, D. Poletti, and M. Mukherjee, Single-atom energy-conversion device with a quantum load, npj Quantum Information 6, 37 (2020).
- [48] H. G. Dehmelt, Slow spin relaxation of optically polarized sodium atoms, Phys. Rev. 105, 1487 (1957).

Supplementary Materials: Computational resource advantage of an ion trap quantum classifier

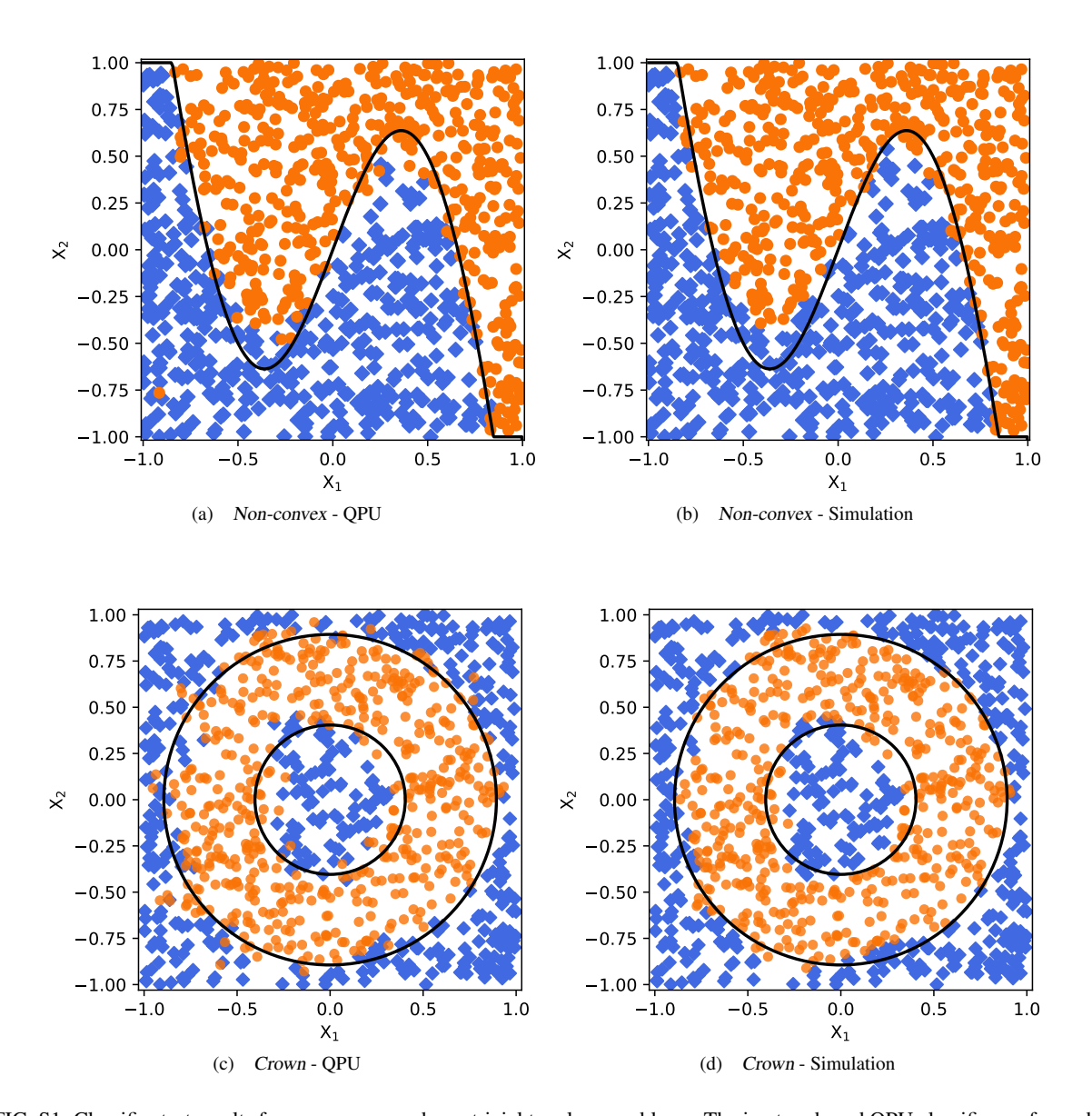


FIG. S1. Classifier test results for non-convex and non-trivial topology problems. The ion trap based QPU classifier performed on 1000 random test data points is depicted in blue for points within and orange outside the boundary separating the circular feature shown in solid line. The results *non-convex* and *crown* datasets are computed using 4 layers, both from QPU and simulation. Notice that the border between classes in the experimental results is not as sharply defined as in the simulated classification. This difference is due to the uncertainty of the quantum measurements.

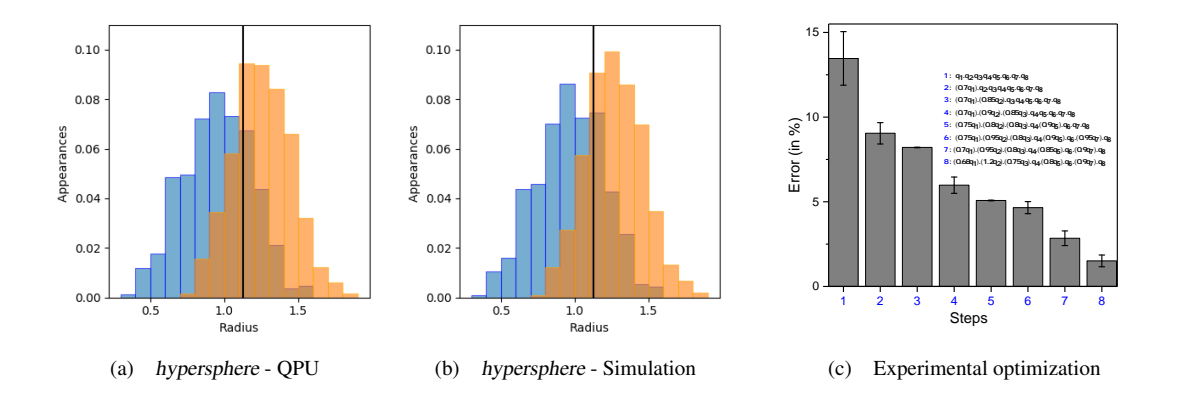


FIG. S2. Binary classification of the *hypersphere* dataset. The histograms in (a) and (b) represent the class association of points within a hyper shell (given by the bin-width) denoted by blue (classified as within the hyper-sphere) and orange (outside the hyper-sphere) for QPU (a) and simulation (b). The overlap region shows the ambiguity in classifying the points within a certain hyper radius. The accuracy of the QPU is improved by performing the experimental optimization near the vicinity of the simulated optima in a series of ten training steps. The reduction in the error with respect to the simulated results (b) is shown in (c).

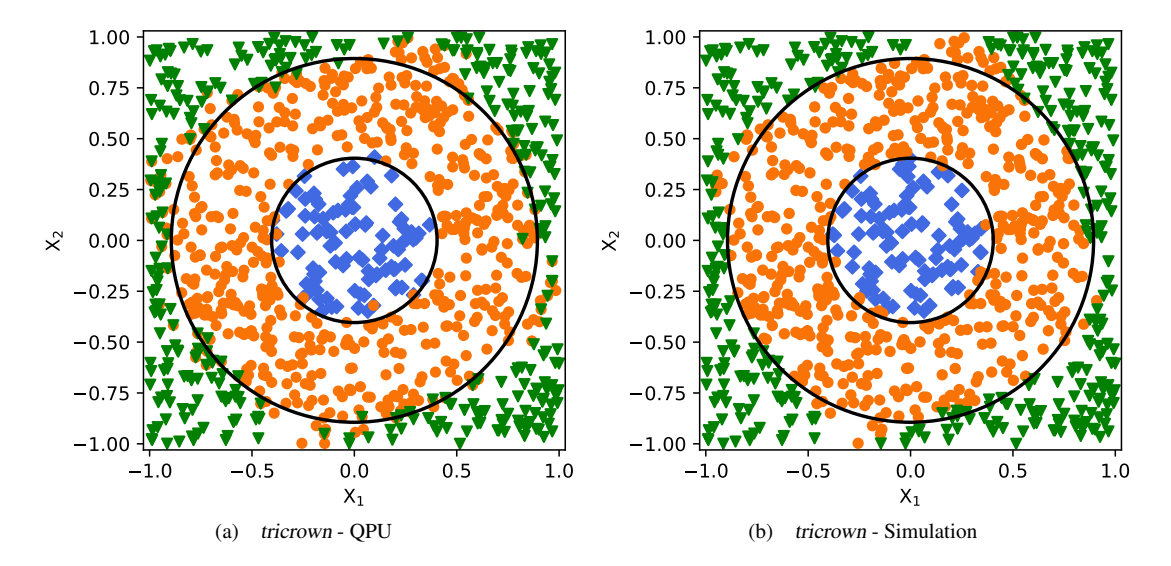


FIG. S3. Multi-class classification for the 3-class *tricrown* problem on the QPU (left) and the simulation (right). Results include 1000 random data points, the classes are depicted in different colors and symbols, and the boundaries are defined by solid black lines. Notice that the border between classes in the experimental results is not as sharply defined as in the simulated classification. This difference is due to the uncertainty of the quantum measurements.